OCT VOLUMETRIC DATA RESTORATION WITH LATENT DISTRIBUTION OF REFRACTIVE INDEX

G. Fujii[†], *Y. Yoshida*[†], *S. Muramatsu*[††,∗], *S. Ono*[‡], *S. Choi*[††,∗], *T. Ota*[§,∗], *F. Nin*[§,∗] *and H. Hibino*[§,∗]

†Graduate School of Science and Tech., Niigata Univ. ††Faculty of Eng., Niigata Univ.
§School of Medicine, Niigata Univ., ‡Dept. of Computer Science, Tokyo Institute of Tech.

ABSTRACT

This work proposes a novel restoration model for optical coherence tomography (OCT) data. The authors have been developing a multi-frequency swept (MS) *en-face* OCT device that can help understand the mechanism of the sensory epithelium in the cochlear. Although the device has merit in acquiring moving tissues, the broadened light gives a weak response; thus, some signal restorations are demanded. This work proposes the introduction of a formulation for OCT data restoration as a convex optimization problem by assuming a latent refractive index distribution. An algorithm to solve the problem with the primal-dual splitting (PDS) framework is then derived. The PDS has an advantage of requiring no inverse matrix operation and being able to handle high-dimensional data. The significance of the proposed model is verified by simulations on artificial data, followed by an experiment with the actual observation of $256 \times 256 \times 2000$ voxels.

***Index Terms*—** Refractive index distribution, primal-dual splitting method, volumetric data, sparse modeling, MS *en-face* OCT

1. INTRODUCTION

The progress of sensing technology in extreme environments is indispensable for the development of science and medicine. As well as hardware devices, physical models and signal processing algorithms need to cooperate together. To measure the vibration of the sensory epithelium *in vivo* and contribute to the treatment of deafness, we are developing an MS *en-face* optical coherence tomography (OCT) device that instantaneously captures the XY plane and acquires a tomographic image by optically scanning the Z direction [1]. Fig. 1 briefly shows the MS *en-face* OCT device configuration.

OCT is a tomographic technique with a spatial resolution in a few μm scale using a near infrared laser [2]. The structure of a target object is measured by the interference between the reference light and the one reflected by the object. Typical OCT techniques, such as Doppler spectral domain (SD) OCT [3–6], acquire tomographic data in the Z direction at a point in the XY plane, and need mechanical 2D scanning in the X and Y directions to construct 3D volumetric data. Compared with others, MS *en-face* OCT has an advantage of being able to observe a dynamic tomographic structure [7]. However, light is broadened by the interference microscope; hence, the light intensity to the image sensor becomes quite weak. As a result, the acquired interference is prone to hide in severe noise.

The denoising of the OCT volumetric data is modeled as a signal restoration problem. In [8], we proposed a denoising method for the OCT data with the iterative hard-thresholding algorithm. Reference [9] proposes a super-resolution technique for retina SD-OCT to shorten the acquisition time. Moreover, [10] proposes a speckle denoising method for retina SD-OCT. However, none of the above-mentioned techniques considered the measurement process (i.e., observation through the interference).

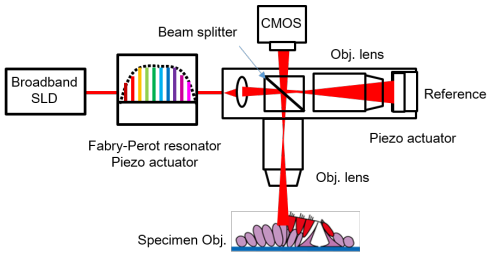

Fig. 1. The MS *en-face* OCT device uses a broadband superluminescent diode (SLD) light source, where a Fabry-Perot resonator is used to generate a multi-wavelength optical comb. The interference peak position is scanned in the Z direction by controlling the frequency interval of the spectrum comb with a piezo actuator. The optical comb is divided into a reference and sample beam by the beam splitter. The field of view is enlarged by the objective lenses, and the reflected lights are formed on the CMOS sensor. The interference between the reference and the sample beam is acquired.

In [11], we proposed a method based on the primal-dual plug-and-play (PDPnP) method [12] to restore the OCT data by considering the measurement process and the range of reflection ratio. PDPnP relies on the PDS algorithm [13, 14], and has an advantage of requiring no inverse matrix operation. Meanwhile, the alternating direction method of multipliers (ADMM) [15,16], which is a popular alternative of the PDS algorithm [17], works with matrix inversion. Although the PDS requires a relatively large number of iterations, it is highly versatile and suitable for processing high-dimensional data such as tomographic images.

In this work, we propose the modification of the problem setting in [11] under the condition that PDS still works. The previous model only considers the structure of the reflective positions, and is likely to fail the estimation. The OCT response to a reflective surface has the shape of a local oscillation similar to the cosine modulated Gaussian function. Unfortunately, many sparse solutions of reflective surface combinations yield a similar oscillating response, which makes it difficult to capture an accurate target structure. In order to overcome this difficulty by introducing a latent refractive index distribution to the model because the distribution is related to the reflective positions and the spatial correlation can be used as an additional regularization.

∗ Advanced Research and Development Programs for Medical Innovation, AMED-CREST

This work was supported by AMED-CREST and JSPS KAKENHI grant number JP16H03164, 19H04135, and 19H02151.

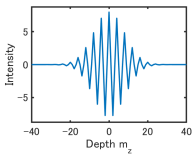

Fig. 2. Discrete model of the coherence function defined by (2), where the amplitude, standard deviation and angular frequency are set to $\alpha_{\rm p} = 8$, $\sigma_{\rm p} = 8$, and $\omega_{\rm p} = 0.25\pi$, respectively.

2. REVIEW OF THE OCT MEASUREMENT MODEL

In this section, let us review the model of the OCT measurement process, and discuss its relation to the refractive index distribution. In the following discussion, we assume that light travels along the Z-axis.

2.1. Observation model

OCT devices acquire tomographic images using the interference between the reference and the sample laser beam (Fig. 1). A discrete model of the OCT observation data $\{t[\mathbf{n}]\}_{\mathbf{n}}$ is modeled as follows

$$t[\mathbf{n}] = b[\mathbf{n}] + \sum_{\mathbf{k}\in\Omega_{\rm r}} r[\mathbf{k}]p[\mathbf{n}-\mathbf{k}] + w[\mathbf{n}],\ \mathbf{n}\in\Omega_{\rm v}, \tag{1}$$

where $\mathbf{n} = [n_{\rm x}, n_{\rm y}, n_{\rm z}]^{\intercal} \in \Omega_{\rm v}$ and $\mathbf{k} = [k_{\rm x}, k_{\rm y}, k_{\rm z}]^{\intercal} \in \Omega_{\rm r}$ are the array indexes of 3D volumetric data. Each element corresponds to the position of horizontal, vertical and depth, respectively [11]. $\Omega_{\rm r}, \Omega_{\rm v} \subset \mathbb{Z}^3$ represent the index domains. $\{b[\mathbf{n}]\}_{\mathbf{n}}$ represents a bias or often trend component in the Z direction that is not a contribution of interference. $\{w[\mathbf{n}]\}_{\mathbf{n}}$ denotes the noise component. $\{p[\mathbf{m}]\}_{\mathbf{m}}$ is an interference waveform (i.e., coherence function) representing the OCT measurement process and has a shape similar to the cosine modulated Gaussian function. $r[\mathbf{k}]$ corresponds to the reflectance distribution of the target object at position $\mathbf{k}\in\Omega_{\rm r}$.

Fig. 2 shows an example of the coherence function $\{p[\mathbf{m}]\}_{\mathbf{m}}$ formulated as:

$$p[\mathbf{m}] = \alpha_{\rm p}\delta[m_{\rm x}]\delta[m_{\rm y}]\exp\left(-\frac{m_{\rm z}^2}{2\sigma_{\rm p}^2}\right)\cos\left(\omega_{\rm p}m_{\rm z}\right),\ \mathbf{m}\in\mathbb{Z}^3, \tag{2}$$

where $\mathbf{m} = [m_{\rm x}, m_{\rm y}, m_{\rm z}]^{\intercal}$, $\alpha_{\rm p}$, $\sigma_{\rm p}$ and $\omega_{\rm p}$ denote amplitude, standard deviation and angular frequency, respectively; and $\delta[m]$ is the impulse sequence defined by 1 for $m = 0$ and 0 for $m \neq 0$.

The reflectance distribution $\{r[\mathbf{k}]\}_{\mathbf{k}}$ is unknown and should be restored from the observation $\{t[\mathbf{n}]\}_{\mathbf{n}}$ to remove the bias $\{b[\mathbf{n}]\}_{\mathbf{n}}$, noise $\{w[\mathbf{n}]\}_{\mathbf{n}}$ and local oscillation by $\{p[\mathbf{m}]\}_{\mathbf{m}}$. Among these degradation factors, the Z direction bias component $\{b[\mathbf{n}]\}_{\mathbf{n}}$ is relatively easy to get rid of by a high-pass filter. Thus, we adopt the following as a restoration target:

$$v[\mathbf{n}] = t[\mathbf{n}] - b[\mathbf{n}],\ \mathbf{n}\in\Omega_{\rm v}. \tag{3}$$

2.2. Reflectance and refractive index

Reflectance is related to refractive index. The reflection ration R at a boundary of different refractive indexes is obtained as follows:

$$R = \frac{|\mathfrak{n}_1 - \mathfrak{n}_2|(\mathfrak{n}_1 - \mathfrak{n}_2)}{(\mathfrak{n}_1 + \mathfrak{n}_2)^2},\ \mathfrak{n}_1, \mathfrak{n}_2 \in [0, \infty), \tag{4}$$

where $\mathfrak{n}_1$ and $\mathfrak{n}_2$ are the refractive indexes of a light incident side and the opposite side, respectively. In (4), the phase shift is also considered, where the sign is determined by their relation. The refractive indexes of the bio-tissues are assumed to have a spatial correlation and be in the range around 1.00 to 1.50.

3. PROPOSED RESTORATION MODEL

Let us propose a novel model to restore the reflectance distribution $\{r[\mathbf{k}]\}_{\mathbf{k}}$ from the observation data $\{v[\mathbf{n}]\}_{\mathbf{n}}$ by using the relation to a latent refractive index distribution.

3.1. Observation model of the OCT device

We consider a latent refractive index distribution $\{u[\mathbf{k}]\}_{\mathbf{k}}$ as the source array for the OCT observation $\{v[\mathbf{n}]\}_{\mathbf{n}}$. Now, let $\mathbf{u} \triangleq \mathrm{vec}(\{u[\mathbf{k}]\}_{\mathbf{k}}) \in \mathbb{R}^N$, $\mathbf{r} \triangleq \mathrm{vec}(\{r[\mathbf{k}]\}_{\mathbf{k}}) \in \mathbb{R}^N$, $\mathbf{v} \triangleq \mathrm{vec}(\{v[\mathbf{n}]\}_{\mathbf{n}}) \in \mathbb{R}^M$ and $\mathbf{w} \triangleq \mathrm{vec}(\{w[\mathbf{n}]\}_{\mathbf{n}}) \in \mathbb{R}^M$, i.e., the vector representations of the latent source, estimation target, observation and noise, respectively, where $N = |\Omega_{\rm r}|$ and $M = |\Omega_{\rm v}|$. For these vector notations, the system with a coherence function $\{p[\mathbf{m}]\}_{\mathbf{m}}$ is represented by matrix $\mathbf{P} \in \mathbb{R}^{M\times N}$. From (1) and (3) with the domain constraint, the observation model is represented as follows:

$$\mathbf{v} = \mathbf{P}\boldsymbol{\phi}(\mathbf{u}) + \mathbf{w},\ \text{s.t. } \mathbf{u}\in[a,b]^N,\ a,b\in\mathbb{R}, \tag{5}$$

where $\mathbf{u}$ is a distribution of the latent refractive index; $[a,b]^N$ denotes the range of $\mathbf{u}$ and $\boldsymbol{\phi}\colon [0,\infty)^N \to (-1,1)^N$ maps the refractive index to that of the reflectance according to the relation in (4) (i.e., $\mathbf{r} = \boldsymbol{\phi}(\mathbf{u})$)[1]. As in [11], we can further assume the generation process of the latent distribution $\mathbf{u}$ by a certain synthesis dictionary $\mathbf{D}\in\mathbb{R}^{N\times L}$ and a coefficient vector $\mathbf{s}\in\mathbb{R}^L$ as

$$\mathbf{u} = \mathbf{D}\mathbf{s}. \tag{6}$$

An advantage of this new model is that hierarchical sparsity regularization can be applied for $\mathbf{r}$ and $\mathbf{s}$ with a hard constraint on $\mathbf{u}$.

From (4), a definition of $\boldsymbol{\phi}(\cdot)$ is given as

$$\boldsymbol{\phi}(\mathbf{u}) = -\mathrm{diag}(\mathrm{abs}(\boldsymbol{\Delta}_{\rm z})\mathbf{u})^{-2}\mathrm{diag}(\mathrm{abs}(\boldsymbol{\Delta}_{\rm z}\mathbf{u}))\boldsymbol{\Delta}_{\rm z}\mathbf{u} \tag{7}$$

where $\boldsymbol{\Delta}_{\rm z}\in\mathbb{R}^{N\times N}$ is a difference operator in the Z-direction.

3.2. Problem setting of the OCT data restoration

As for $\boldsymbol{\Delta}_z$ in (7), this work adopts the following convolutional operator with the impulse response

$$d_{\rm z}[\mathbf{m}] \triangleq \mathcal{Z}^{-1}\left\{(z_{\rm x}+2+z_{\rm x}^{-1})(z_{\rm y}+2+z_{\rm y}^{-1})(z_{\rm z}-z_{\rm z}^{-1})/32\right\},$$

which is an extension of 2D Sobel operator to 3D, where $\mathcal{Z}^{-1}\{\cdot\}$ means the 3D inverse Z-transform. Note that $\boldsymbol{\Delta}_{\rm z}^{\intercal} = -\boldsymbol{\Delta}_{\rm z}$ and $\mathrm{abs}(\boldsymbol{\Delta}_{\rm z}^{\intercal}) = \mathrm{abs}(\boldsymbol{\Delta}_{\rm z})$ hold, where superscript "$^{\intercal}$" denotes its adjoint.

Assuming sparseness on $\boldsymbol{\Delta}_{\rm z}\mathbf{u}$, instead of $\mathbf{r} = \boldsymbol{\phi}(\mathbf{u})$, as well as $\mathbf{s}$, the problem setting is formulated as follows:

$$\hat{\mathbf{s}} = \arg\min_{\mathbf{s}\in\mathbb{R}^L} \frac{1}{2}\|\mathbf{P}\boldsymbol{\phi}(\mathbf{D}\mathbf{s}) - \mathbf{v}\|_2^2 + \lambda\|\mathbf{s}\|_1 + \eta\|\boldsymbol{\Delta}_{\rm z}\mathbf{D}\mathbf{s}\|_1,$$
$$\text{s.t. } \mathbf{D}\mathbf{s}\in[a,b]^N, \tag{8}$$

where $\|\cdot\|_2$ and $\|\cdot\|_1$ are the 2-norm and the 1-norm, respectively; $a, b \in [0,\infty)$ are the lower and upper bounds of $\mathbf{u}$; and $\lambda, \eta \in [0,\infty)$ denote the regularization parameters. The reflectance distribution $\mathbf{r}$ is estimated as $\hat{\mathbf{r}} = \boldsymbol{\phi}(\mathbf{D}\hat{\mathbf{s}})$.

[1] Note that (5) is mathematically reduced to the model in [11] when $\boldsymbol{\phi}(\cdot)$ is identity and $[a,b]^N = [-1,1]^N$.

Algorithm 1 Primal-dual splitting (PDS) algorithm [13]

Input: $\mathbf{x}^{(0)}, \mathbf{y}^{(0)}$
Output: $\mathbf{x}^{(n)}$

while A stopping criterion is not satisfied **do**
  $\mathbf{x}^{(n+1)} = \mathrm{prox}_{\gamma_1 g}\left(\mathbf{x}^{(n)} - \gamma_1(\nabla f(\mathbf{x}^{(n)}) + \mathbf{L}^\mathsf{T}\mathbf{y}^{(n)})\right)$
  $\mathbf{y}^{(n+1)} = \mathrm{prox}_{\gamma_2 h^*}\left(\mathbf{y}^{(n)} + \gamma_2\mathbf{L}(2\mathbf{x}^{(n+1)} - \mathbf{x}^{(n)})\right)$
  $n \leftarrow n+1$
end while

Algorithm 2 PDS for solving the problem in (8)

Input: $\mathbf{x}^{(0)}, \mathbf{y}_1^{(0)}, \mathbf{y}_2^{(0)}$
Output: $\mathbf{x}^{(n)}, \mathbf{q}^{(n)}$

$\mathbf{q}^{(0)} = \mathbf{D}\mathbf{x}^{(0)}$
while A stopping criterion is not satisfied **do**
  $\mathbf{t} \leftarrow \mathbf{D}^\mathsf{T}(\nabla\mathcal{F}(\mathbf{q}^{(n)}) + \boldsymbol{\Delta}_z^\mathsf{T}\mathbf{y}_1^{(n)} + \mathbf{y}_2^{(n)})$
  $\mathbf{x}^{(n+1)} = \mathfrak{G}_{\lambda\|\cdot\|_1}(\mathbf{x}^{(n)} - \gamma_1\mathbf{t}, \gamma_1^{\frac{1}{2}})$
  $\mathbf{q}^{(n+1)} = \mathbf{D}\mathbf{x}^{(n+1)}$
  $\mathbf{u} \leftarrow 2\mathbf{q}^{(n+1)} - \mathbf{q}^{(n)}$
  $\mathbf{y}_1^{(n)} \leftarrow \mathbf{y}_1^{(n)} + \gamma_2\boldsymbol{\Delta}_z\mathbf{u}$
  $\mathbf{y}_2^{(n)} \leftarrow \mathbf{y}_2^{(n)} + \gamma_2\mathbf{u}$
  $\mathbf{y}_1^{(n+1)} = \mathbf{y}_1^{(n)} - \gamma_2\mathfrak{G}_{\eta\|\cdot\|_1}(\gamma_2^{-1}\mathbf{y}_1^{(n)}, \gamma_2^{-\frac{1}{2}})$
  $\mathbf{y}_2^{(n+1)} = \mathbf{y}_2^{(n)} - \gamma_2 P_{[a,b]^N}(\gamma_2^{-1}\mathbf{y}_2^{(n)})$
  $n \leftarrow n+1$
end while

3.3. Linear approximation of $\phi(\cdot)$

Although the original $\phi(\cdot)$ in (7) is differentiable, it is non-linear and violates the convexity of the problem in (8). Thus, we propose to linearly approximate $\phi(\cdot)$ for the domain assumed to the refractive index. Our linear approximation of $\phi(\cdot)$ is as follows:

$$\boldsymbol{\phi}_1(\mathbf{u}) = -\beta_1(a,b)\boldsymbol{\Delta}_z\mathbf{u}, \tag{9}$$

where $\beta_1(a,b) = 2|b-a|/(b+a)^2$ is derived from (4) and the gain of $\{d_z[\mathbf{m}]\}_\mathbf{m}$ in the Z-direction. Equation (9) guarantees that the response is null when $\mathfrak{n}_1 = \mathfrak{n}_2$ and $\mathbf{r} = \boldsymbol{\phi}_1(\mathbf{u}) \in (-1,1)^N$.

The derivative of $\boldsymbol{\phi}_1(\cdot)$ with respect to $\mathbf{u}$ is given as

$$\frac{\partial\boldsymbol{\phi}_1}{\partial\mathbf{u}} = -\beta_1(a,b)\boldsymbol{\Delta}_z = \beta_1(a,b)\boldsymbol{\Delta}_z^\mathsf{T}, \tag{10}$$

where $[\partial\mathbf{f}/\partial\mathbf{x}]_{n,m} \triangleq \partial[\mathbf{f}]_n/\partial[\mathbf{x}]_m$. $[\cdot]_n$ and $[\cdot]_{n,m}$ denote the nth element of the vector and the n,mth element of the matrix, respectively.

3.4. Restoration algorithm

Let us adopt the PDS algorithm to solve the problem in (8). The algorithm can solve problems in the following form:

$$\hat{\mathbf{x}} = \arg\min_{\mathbf{x}\in\mathbb{R}^L} f(\mathbf{x}) + g(\mathbf{x}) + h(\mathbf{L}\mathbf{x}), \tag{11}$$

where $f\colon \mathbb{R}^L \to \mathbb{R}\cup\{\infty\}$, $g\colon \mathbb{R}^L \to \mathbb{R}\cup\{\infty\}$ and $h\colon \mathbb{R}^K \to \mathbb{R}\cup\{\infty\}$ are the proper lower semi-continuous convex functions; $\nabla f(\cdot)$ is the μ-Lipschitz continuous; and $\mathbf{L}\in\mathbb{R}^{K\times L}$.

Algorithm 1 shows the steps of the PDS [13]. Symbols γ_1 and γ_2 are the step size parameters set to satisfy $\gamma_1^{-1} - \gamma_2(\sigma_{\max}(\mathbf{L}))^2 \geq \mu/2$, where $\sigma_{\max}(\mathbf{L})$ is the maximum singular value of $\mathbf{L}$ [13].

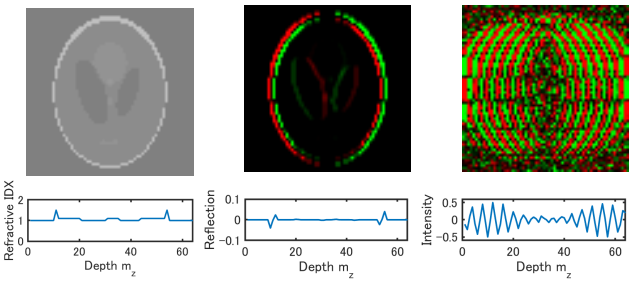

(a) (b) (c)

Fig. 3. Example set of the artificial volumetric arrays. (Top) YZ slice at the center of X. (Bottom) Z direction sequence at the center of the XY plane. (a) Latent refractive index distribution $\mathbf{u}$ of $16\times64\times64$ voxels, where the `phantom` function of MATLAB R2018a is used with the option "Modified Shepp-Logan". The intensity is scaled to the range between $a = 1.00$ and $b = 1.50$. The YZ slice is replicated to the X direction. (b) Reflective distribution $\mathbf{r}$ derived from $\mathbf{u}$ by using the mapping $\boldsymbol{\phi}(\cdot)$ in (7). (c) Observation $\mathbf{v}$, where the function in Fig. 2 is set to the measurement process as $\mathbf{P}$. The AWGN of the zero mean and standard deviation of 4×10^{-2} is set as noise $\mathbf{w}$. The green and red voxels denote the positive and negative values, respectively.

To apply the PDS algorithm to the problem in (8), let

$$f(\mathbf{x}) = \mathcal{F}(\mathbf{D}\mathbf{x}) = \frac{1}{2}\|\mathbf{P}\boldsymbol{\phi}_1(\mathbf{D}\mathbf{x}) - \mathbf{v}\|_2^2, \tag{12a}$$

$$g(\mathbf{x}) = \lambda\|\mathbf{x}\|_1, \tag{12b}$$

$$h(\mathbf{L}\mathbf{x}) = \eta\|\mathbf{y}_1\|_1 + \imath_{[a,b]^N}(\mathbf{y}_2), \tag{12c}$$

$$\mathbf{L}\mathbf{x} = \begin{bmatrix}\mathbf{y}_1\\ \mathbf{y}_2\end{bmatrix} = \begin{bmatrix}\boldsymbol{\Delta}_z\mathbf{D}\\ \mathbf{D}\end{bmatrix}\mathbf{x}. \tag{12d}$$

We then obtain the PDS steps with the hierarchical sparsity with a hard constraint (Algorithm 2). If synthesis dictionary $\mathbf{D}$ satisfies the Parseval tightness (i.e., $\mathbf{D}\mathbf{D}^\mathsf{T} = \mathbf{I}$ [18, 19]), then $\sigma_{\max}(\mathbf{L}) = \sigma_{\max}\left(\left[\begin{smallmatrix}\boldsymbol{\Delta}_z\\ \mathbf{I}\end{smallmatrix}\right]\right)$ holds, where $\mathbf{I}$ is the identity matrix. For example, orthonormal transforms, namely the undecimated Haar transform (UDHT) [20] and nonseparable oversampled lapped transform (NSOLT) [21] satisfy the Parseval tight condition.

In Algorithm 2, $\mathfrak{G}_{\lambda\|\cdot\|_1}(\mathbf{x},\sigma)$ and $P_{[a,b]^N}(\mathbf{x})$ denote soft-thresholding and metric projection defined as follows:

$$\left[\mathfrak{G}_{\lambda\|\cdot\|_1}(\mathbf{x},\sigma)\right]_n \triangleq \mathrm{sgn}([\mathbf{x}]_n)\max\left\{|[\mathbf{x}]_n| - \lambda\sigma^2, 0\right\}, \tag{13}$$

$$\left[P_{[a,b]^N}(\mathbf{x})\right]_n \triangleq \min\{\max\{[\mathbf{x}]_n, a\}, b\}. \tag{14}$$

The gradient of $\mathcal{F}(\cdot)$ is obtained by the chain rule as

$$\nabla\mathcal{F}(\mathbf{u}) = \left(\frac{\partial\boldsymbol{\phi}_1}{\partial\mathbf{u}}\right)^\mathsf{T}\mathbf{P}^\mathsf{T}(\mathbf{P}\boldsymbol{\phi}_1(\mathbf{u}) - \mathbf{v}). \tag{15}$$

The Lipschitz constant of $\nabla f(\cdot)$ is $\mu = (\beta_1(a,b)\sigma_{\max}(\mathbf{P}\boldsymbol{\Delta}_z\mathbf{D}))^2$.

4. PERFORMANCE EVALUATION

In this section, let us verify the significance of the proposed model by simulations on artificial data. We then show the experimental result for an observation array of the sensory epithelium of a guinea pig's inner ear measured by the MS *en-face* OCT device.

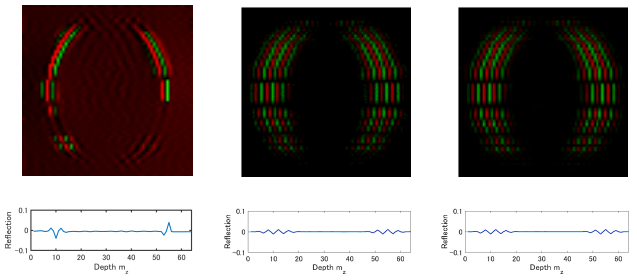

(a) (b) (c)

Fig. 4. Restoration results of the reflectance distribution $\mathbf{r}$. (Top) YZ slice of reflection at the center of X. (Bottom) Z direction sequence at the center of the XY plane. (a) Previous method using $\mathbf{D} = \mathbf{I}$ and BM4D in [11], where MSE=3.82×10^{-5}. (b) Proposed method using $\mathbf{D} = \mathbf{I}$ and BM4D in Step 4, where MSE: 2.26×10^{-5}. (c) Proposed method using UDHT as $\mathbf{D}$ and soft-thresholding in Step 4, where MSE: 2.26×10^{-5}. The array in Fig. 3 (c) is used as observation $\mathbf{v}$. The parameters are set as $\gamma_1 = 3.0941 \times 10^{-4}$ and $\gamma_2 = 76.1905$. ♯ of iterations is set to 1000.

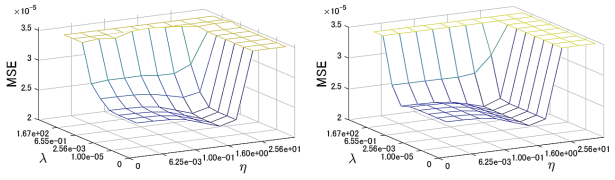

(a) (b)

Fig. 5. MSE validation for sparse regularization parameters λ and η. (a) Proposed method using $\mathbf{D} = \mathbf{I}$ and BM4D in Step 4. (b) Proposed method using UDHT as $\mathbf{D}$ and soft-thresholding in Step 4.

4.1. Restoration simulation

We verify the significance of the proposed method in (8) by comparing the restoration result with that of the previous method in [11], where, for reference, we also show the result of using BM4D [22] as a regularized Gaussian denoiser in Step 4 in a similar way to [11,12]. Figs. 3 (a), (b) and (c) illustrate the artificial refractive index distribution $\mathbf{u}$, reflectance distribution $\mathbf{r}$, and an observation $\mathbf{v}$ measured through the coherence function shown in Fig. 2, respectively.

The simulation configuration is as follows:

- Combination of dictionary $\mathbf{D}$ and Gaussian denoiser $\mathfrak{G}_{\mathcal{R}}(\cdot, \sigma)$:
  - Identity map ($\mathbf{D} = \mathbf{I}$) and BM4D [22]
  - 3D UDHT [20] and soft-thresholding in (13)
- Step-size parameters:
  - $\gamma_1 = 2/(1.05\mu) \approx 3.0941 \times 10^{-4}$
  - $\gamma_2 = (1.05\xi)^{-1}(1/\gamma_1 - \mu/2)$, where $\xi = (\sigma_{\max}(\mathbf{L}))^2$
- The number of iterations is set to 1000.

Note that $\sigma_{\max}(\mathbf{L}) = \sqrt{\lambda_{\max}(\mathbf{\Delta}_z^{\mathsf{T}}\mathbf{\Delta}_z) + 1}$ for a Parseval tight dictionary $\mathbf{D}$, where $\lambda_{\max}(\cdot)$ denotes the maximum eigenvalue.

Figs. 4 and 5 show the restoration results and the MSE valiation for sparse regularization parameters λ and η. Fig. 4 (a) depicts the result of the previous model in [11]. Figs. 4 (b) and (c) represent the result using BM4D and that using UDHT and soft-thresholding, respectively, where λ and η are selected as the best values from Fig. 5.

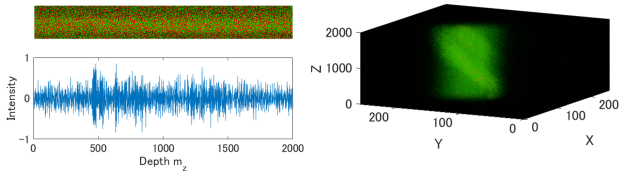

Fig. 6. Observation $\mathbf{v}$ of the sensory epithelium of a guinea pig's inner ear measured by the MS *en-face* OCT device. (Left top) YZ slice at the center of X. (Left bottom) Z direction sequence at the center of XY. (Right) 3D representation of size $256 \times 256 \times 2000$ voxel corresponding to physical dimension of $1 \times 1 \times 0.15\mathrm{mm}^3$. The output of the average filter of length 21 is subtracted from the original as a pre-processing to remove the Z direction bias or trend component.

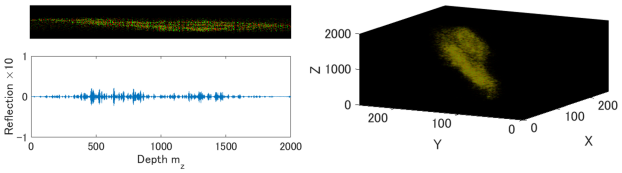

Fig. 7. Restored result $\hat{\mathbf{r}} = \phi_1(\mathbf{D}\hat{\mathbf{s}})$ using UDHT as $\mathbf{D}$, where the intensity is emphasized. (Left top) YZ slice at the center of X. (Left bottom) Z direction sequence at the center of XY. (Right) 3D representation. ♯ of iterations is set to 1000.

Fig. 4 (b) and (c) show a better performance compare to the previous method in (a) and almost the same performance as each other. The combination of UDHT and soft-thresholding is faster than BM4D. The effect of introducing the regularization and constraint for the OCT model is confirmed.

4.2. Restoration experiment

Let us adopt the proposed method with the combination of UDHT and soft-thresholding. Fig. 6 shows an observation of the sensory epithelium of a guinea pig's inner ear measured by an MS *en-face* OCT device. Fig. 7 exhibits the restoration result, where the model in Fig. 2 was experimentally set for the observation process $\mathbf{P}$, and the setting similar to the simulation in Section 4.1 is adopted. The data size is $256 \times 256 \times 2000$ voxels, which corresponds to a physical dimension of $1 \times 1 \times 0.15\ \mathrm{mm}^3$.

The proposed method is capable of handling high-volume OCT data with a high quality restoration performance.

5. CONCLUSIONS

This study proposed the introduction of a latent refractive distribution for the OCT volumetric data restoration. We reduced the restoration problem to a sparsity-aware least square minimization with a hard constraint and constructed an algorithm to solve the problem based on the PDS framework. The significance was verified by the simulations on the artificial data and an experiment on the actual MS *en-face* OCT measurement data. Although the main motivation of this work is to overcome the weakness of the MS *en-face* OCT device, the proposed model is also available for the others. The restoration based on the proposed model is expected to reduce the laser power of OCT devices, while keeping the acquisition performance.

6. REFERENCES

[1] J. M. Schmitt, "Optical coherence tomography (OCT): a review," *IEEE Journal of Selected Topics in Quantum Electronics*, vol. 5, no. 4, pp. 1205–1215, Jul 1999.

[2] S. Apostolopoulos and R. Sznitman, "Efficient OCT volume reconstruction from slitlamp microscopes," *IEEE Transactions on Biomedical Engineering*, vol. 64, no. 10, pp. 2403–2410, Oct 2017.

[3] D. M. Freeman S. S. Hong, "Doppler optical coherence microscopy for studies of cochlear mechanics," *Journal of Biomedical Optics*, vol. 11, pp. 11 – 11 – 5, 2006.

[4] S. S. Gao, R. Wang, P. D. Raphael, Y. Moayedi, A. K. Groves, J. Zuo, B. E. Applegate, and J. S. Oghalai, "Vibration of the organ of corti within the cochlear apex in mice," *Journal of Neurophysiology*, vol. 112, no. 5, pp. 1192–1204, 2014.

[5] S. S. Gao, P. D. Raphael, R. Wang, J. Park, A. Xia, B. E. Applegate, and J. S. Oghalai, "In vivo vibrometry inside the apex of the mouse cochlea using spectral domain optical coherence tomography," *Biomed. Opt. Express*, vol. 4, no. 2, pp. 230–240, Feb 2013.

[6] B. E. Applegate, R. L. Shelton, S. S. Gao, and J. S. Oghalai, "Imaging high-frequency periodic motion in the mouse ear with coherently interleaved optical coherence tomography," *Opt. Lett.*, vol. 36, no. 23, pp. 4716–4718, Dec 2011.

[7] S. Choi, T. Watanabe, T. Suzuki, F. Nin, H. Hibino, and O. Sasaki, "Multifrequency swept common-path en-face OCT for wide-field measurement of interior surface vibrations in thick biological tissues," *Opt. Express*, vol. 23, no. 16, pp. 21078–21089, Aug 2015.

[8] S. Muramatsu, S. Choi, and T. Kawamura, "3-D OCT data denoising with nonseparable oversampled lapped transform," in *2015 Asia-Pacific Signal and Information Processing Association Annual Summit and Conference (APSIPA)*, Dec 2015, pp. 901–906.

[9] L. Fang, S. Li, R. P. McNabb, Q. Nie, A. N. Kuo, C. A. Toth, J. A. Izatt, and S. Farsiu, "Fast acquisition and reconstruction of optical coherence tomography images via sparse representation," *IEEE Transactions on Medical Imaging*, vol. 32, no. 11, pp. 2034–2049, Nov 2013.

[10] J. Cheng, D. Tao, Y. Quan, D. W. K. Wong, G. C. M. Cheung, M. Akiba, and J. Liu, "Speckle reduction in 3D optical coherence tomography of retina by a-scan reconstruction," *IEEE Transactions on Medical Imaging*, vol. 35, no. 10, pp. 2270–2279, Oct 2016.

[11] S. Muramatsu, S. Choi, S. Ono, T. Ota, F. Nin, and H. Hibino, "OCT volumetric data restoration via prima-dual plug-and-play method," in *2018 IEEE International Conference on Acoustics, Audio and Signal Processing (ICASSP)*, Apr. 2018, pp. 801–805.

[12] S. Ono, "Primal-dual plug-and-play image restoration," *IEEE Signal Processing Letters*, vol. 24, no. 8, pp. 1108–1112, Aug 2017.

[13] L. Condat, "A primal–dual splitting method for convex optimization involving Lipschitzian, proximable and linear composite terms," *Journal of Optimization Theory and Applications*, vol. 158, no. 2, pp. 460–479, Aug 2013.

[14] S. Ono and I. Yamada, "Hierarchical convex optimization with primal-dual splitting," *IEEE Transactions on Signal Processing*, vol. 63, no. 2, pp. 373–388, Jan 2015.

[15] J. Eckstein and D. P. Bertsekas, "On the Douglas—Rachford splitting method and the proximal point algorithm for maximal monotone operators," *Mathematical Programming*, vol. 55, no. 1, pp. 293–318, Apr 1992.

[16] D. Gabay and B. Mercier, "A dual algorithm for the solution of nonlinear variational problems via finite element approximation," *Computers & Mathematics with Applications*, vol. 2, no. 1, pp. 17 – 40, 1976.

[17] R. G. Baraniuk, T. Goldstein, A. C. Sankaranarayanan, C. Studer, A. Veeraraghavan, and M. B. Wakin, "Compressive video sensing: Algorithms, architectures, and applications," *IEEE Signal Processing Magazine*, vol. 34, no. 1, pp. 52–66, Jan 2017.

[18] J. Kovačević and A. Chebira, "Life beyond bases: The advent of frames (part i)," *IEEE Signal Processing Magazine*, vol. 24, no. 4, pp. 86–104, July 2007.

[19] J. L. Starck, F. Murtagh, and J. Fadili, *Sparse Image and Signal Processing: Wavelets and Related Geometric Multiscale Analysis*, Cambridge University Press, 2015.

[20] M. Unser, "Texture classification and segmentation using wavelet frames," *IEEE Transactions on Image Processing*, vol. 4, no. 11, pp. 1549–1560, Nov 1995.

[21] S. Muramatsu, K. Furuya, and N. Yuki, "Multidimensional nonseparable oversampled lapped transforms: Theory and design," *IEEE Transactions on Signal Processing*, vol. 65, no. 5, pp. 1251–1264, March 2017.

[22] K. Dabov, A. Foi, V. Katkovnik, and K. Egiazarian, "Image denoising by sparse 3-D transform-domain collaborative filtering," *IEEE Transactions on Image Processing*, vol. 16, no. 8, pp. 2080–2095, Aug 2007.